J. Fluid Mech. (2016), *vol.* 800, *pp.* 595–612. © Cambridge University Press 2016
doi:10.1017/jfm.2016.364

The flow dynamics of the garden-hose instability

Fangfang Xie[1], Xiaoning Zheng[1], Michael S. Triantafyllou[1], Yiannis Constantinides[2] and George Em Karniadakis[3],†

[1]Department of Mechanical Engineering, Massachusetts Institute Technology, Cambridge, MA 02139, USA

[2]Chevron Energy Technology Company, Houston, TX 77002, USA

[3]Division of Applied Mathematics, Brown University, Providence, RI 02912, USA

(Received 9 September 2015; revised 2 April 2016; accepted 27 May 2016; first published online 12 July 2016)

We present fully resolved simulations of the flow–structure interaction in a flexible pipe conveying incompressible fluid. It is shown that the Reynolds number plays a significant role in the onset of flutter for a fluid-conveying pipe modelled through the classic garden-hose problem. We investigate the complex interaction between structural and internal flow dynamics and obtain a phase diagram of the transition between states as function of three non-dimensional quantities: the fluid-tension parameter, the dimensionless fluid velocity and the Reynolds number. We find that the flow patterns inside the pipe strongly affect the type of induced motion. For unsteady flow, if there is symmetry along a direction, this leads to in-plane motion whereas breaking of the flow symmetry results in both in-plane and out-of-plane motions. Hence, above a critical Reynolds number, complex flow patterns result for the vibrating pipe as there is continuous generation of new vorticity due to the pipe wall acceleration, which is subsequently shed in the confined space of the interior of the pipe.

Key words: bifurcation, flow–structure interactions, vortex flows

1. Introduction

A flexible, fluid-conveying pipe constitutes a simple flow–structure interaction system with intriguingly complex dynamical properties. Such systems are extensively used in the oil and gas industry and in nuclear engineering but are also of great interest in biomechanics, e.g. the blood flow in veins or air flow in pulmonary alveoli. A flutter instability arises if the fluid velocity in the pipe is sufficiently high, resulting in a pipe motion whose form is close to a sinusoidal one at lower velocity values, while it appears totally erratic at higher velocities. This is an instability that we can observe in everyday life, such as when watering the garden with a hose (hence the name garden-hose or water-hose instability), or watching ‘sky dancers’ – long flexible tubes dancing above air blowers in the streets to advertise a product (Doaré & De Langre 2002; Cros, Romero & Flores 2012).

Bourrières (1939) was one of the first to conduct experiments to determine the flutter of a cantilevered pipe; a similar study was undertaken later by Ashley &

† Email address for correspondence: george_karniadakis@brown.edu

Haviland (1950) in order to explain the vibrations of long pipelines. Benjamin (1961*a*,*b*) derived the general theory of fluid-conveying flexible pipes and shed light on the principal mechanisms of flow–structure interaction. In their pioneering work, Paidoussis and his collaborators (Gregory & Paidoussis 1966; Paidoussis 1998, 2004) have elucidated the onset of the instabilities that appear in fluid-conveying systems in a series of publications combining experimental and theoretical studies.

In previous studies, the focus has been mainly on the dynamics of the pipe using approximate flow models, whereas the fully resolved viscous flow dynamics inside the pipe, to the best of our knowledge, has never been studied systematically when coupled with the pipe vibrations (for the flow inside the pipe, we perform direct numerical simulations based on the three-dimensional incompressible Navier–Stokes equations for viscous fluids). Typically, the flow effect has been modelled through potential flow analysis, *viz.* through the added mass forces acting on the pipe. Similarly, depending on whether the flow is laminar or turbulent, Guo, Zhang & Païdoussis (2010) proposed various flow profile modification factors to consider the non-uniformity of the flow velocity distribution, however, the fluid dynamics in the pipe was still over-simplified. As we know, flow in a stationary pipe transitions to turbulence at a Reynolds number of approximately $Re \approx 2000$, but oscillations of the pipe greatly affect the flow patterns, lowering substantially the transition point (Benhamou, Laneville & Galanis 2004). We demonstrate this flow sensitivity on the amplitude of the transverse oscillation, through simulation of the flow in a circular pipe subjected to a planar motion in the form of a standing wave at two different amplitudes: (*a*) $A = 0.5D$, (*b*) $A = 1.0D$. The motion of the pipe is prescribed as: $y = A\ \sin(2\pi ft)\ \sin(2\pi z/L)$, with frequency $f = 0.167$, pipe length $L = 15D$ and diameter D. A constant body force is used to drive the flow at mean Reynolds number $Re = 800$. From figure 1 we note that, while the flow remains laminar at the lower amplitude, at the higher amplitude there is clear evidence of transition. If the pipe is free to move under the action of fluid forces, we find that this new flow state induces amplification of the oscillation, which will further excite the flow, and so on, forming an unstable feedback loop.

We study the internal flow-induced vibration of the pipe via direct numerical simulation (DNS), in parallel with eigenvalue analysis of the corresponding simplified problem. The coupled fluid–structure system is solved using the research spectral element code NEKTAR (Karniadakis & Sherwin 2013), employing a Fourier expansion in the z flow direction and a tensor-product Jacobi polynomial basis in the cross-flow (x, y) planes. For the fluid, the Navier–Stokes equations are solved while for the structure solver a tensioned beam equation is used. Moreover, a boundary-fitted coordinate formulation is used to take into account the pipe unsteady deformation. Since this solver has been used extensively in simulating vortex-induced vibration of a cylinder in external flow (Newman & Karniadakis 1997; Evangelinos & Karniadakis 1999; Bourguet, Karniadakis & Triantafyllou 2011, 2013), we do not repeat all the details here; we refer the interested readers to Newman & Karniadakis (1997).

The paper is organized as follows. Section 2 describes the physical model of a fluid-conveying pipe under the boundary conditions of the classic garden-hose problem. We propose and justify a 'discontinuous' forcing model to study the flow-induced instability mechanism, both for the system employing DNS and for the eigenvalue analysis of the system employing a simplified flow model. In § 3, we provide the simulation results of the fluid dynamics and structural dynamics. We first compare the difference between a 'full' forcing model and a 'discontinuous' forcing model in § 3.1. Then we present a phase diagram of dynamic transition between states as function

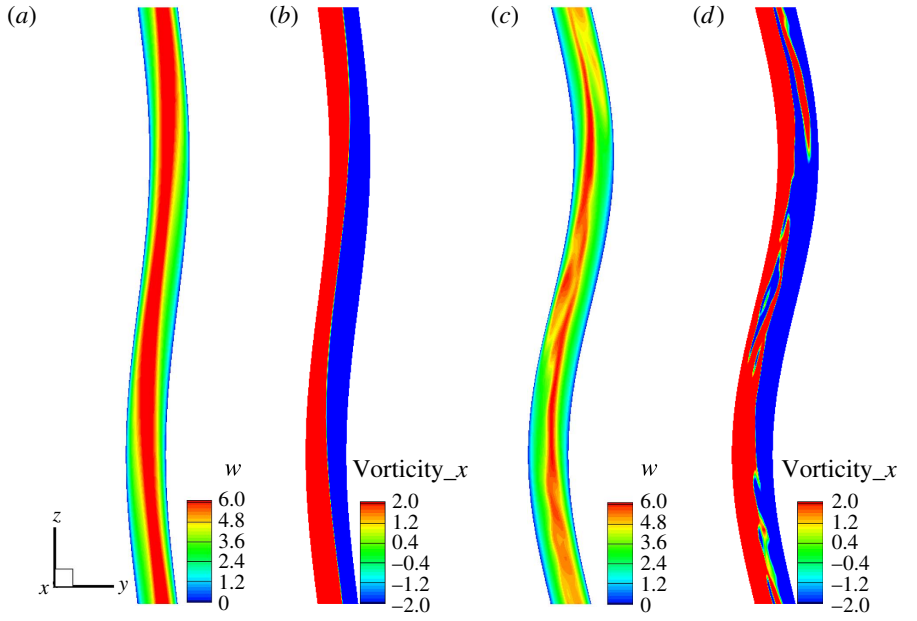

FIGURE 1. (Colour online) Flow transition at subcritical Reynolds number. Instantaneous contours of axial velocity (*a*,*c*) and vorticity perpendicular to the plane of motion (*b*,*d*) at the mid-plane of an oscillating pipe under different amplitudes. (*a*,*b*) $A = 0.5D$, (*c*,*d*) $A = 1.0D$. The motion of the pipe is prescribed as: $y = A\sin(2\pi ft)\sin(2\pi z/L)$, with $f = 0.167$ the frequency, $L = 15D$ the pipe length and D the diameter. A constant body force is used to drive the flow at mean Reynolds number $Re = 800$.

of three non-dimensional parameters in § 3.2. Moreover, we obtain the bifurcation diagrams for both the flow and the structure quantitatively, and also compare the DNS results against the eigenvalue analysis in § 3.3. Finally, we summarize the main points of our paper in § 4.

2. System models

The fluid-conveying pipe with circular cross-section is parametrized by the pipe length L, diameter D, structural mass per unit length m_c, flexural rigidity EI and tension T. The fluid is characterized by its density ρ_f, dynamic viscosity μ, conveying fluid mass per unit length $m_a = \rho_f(\pi D^2/4)$ and a mean axial flow velocity U. The mass ratio between solid and fluid is $(m_c/m_a) = 24/\pi$ for the results reported in this study, but other values were investigated. The Reynolds number Re is defined as $Re = \rho_f UD/\mu$. The units for these variables can be seen in table 1.

The structural dynamics is represented by a string-beam model, expressed as:

$$m_c\frac{\partial^2 q}{\partial t^2} = \frac{\partial}{\partial s}\left(T\frac{\partial q}{\partial s}\right) - \frac{\partial^2}{\partial s^2}\left(EI\frac{\partial^2 q}{\partial s^2}\right) + \tilde{F}, \tag{2.1}$$

where s is the Lagrangian coordinate along the pipe; $q = [q_x, q_y]^{\mathrm{T}}$ and $\tilde{F} = [\tilde{F}_x, \tilde{F}_y]^{\mathrm{T}}$ denote the motions in a plane locally perpendicular to the axis of the pipe and the corresponding forces from the fluid side, respectively.

	T	EI	Re	u	I_p
Units	kg m s^{-2}	kg m^{-3} s^{-2}	1	1	1
Case 1	3	120	740	7.9	1.4
Case 2	13.2	120	1330	14.2	0.998
Group 3	13.2	120	[646, 1330]	[2.15, 4.4]	[0.24, 0.998]

TABLE 1. Physical parameters used in the current paper.

2.1. *Structure model set-up*

A clamp-free cantilever pipe model was used to simulate the garden-hose problem in previous studies. In the current simulations, we employ a different set-up in order to facilitate the three-dimensional (3-D) flow computations, an approach we call the 'discontinuous' forcing model. We employ periodicity conditions along the flow direction, with pinned–pinned pipe end conditions. In order to effectively study a cantilevered pipe, we apply the forces from the fluid solver only over a segment of the pipe, starting from one end and ending somewhere before the other end; hence a 'discontinuous' forcing is applied. To justify the model selection, we analyse the work, W_T, done by fluid forces over one oscillation cycle of pipe, modelled through the added mass effect (Ibrahim 2010), which is:

$$\begin{aligned} W_T &= -\int_0^T \int_0^L m_a \left(\frac{\partial^2 q}{\partial t^2} + 2U \frac{\partial^2 q}{\partial t \partial s} + U^2 \frac{\partial^2 q}{\partial s^2} \right) \frac{\partial q}{\partial t} \, \mathrm{d}s \, \mathrm{d}t \\ &= -m_a \left(\int_0^L \left(\left[\frac{1}{2} \left(\frac{\partial q}{\partial t} \right)^2 \right]_0^T - U^2 \left[\frac{1}{2} \left(\frac{\partial q}{\partial s} \right)^2 \right]_0^T \right) \mathrm{d}s \right. \\ &\quad \left. + U \int_0^T \left(\left[\left(\frac{\partial q}{\partial t} \right)^2 \right]_0^L + U \left[\left(\frac{\partial q}{\partial s} \frac{\partial q}{\partial t} \right) \right]_0^L \right) \mathrm{d}t \right). \end{aligned} \tag{2.2}$$

For a periodic motion, the first two terms vanish. For a pinned–pinned pipe with forcing over the entire length, the total work is zero, since both ends are fixed: $\partial q/\partial t(0) = \partial q/\partial t(L) = 0$. Hence the fluid force does not supply any net energy to the pipe, and there can be no flutter instability in this case due to the end conditions. Note that the argument here is somewhat circular as far as the stability of the overall pipe is concerned, because we assumed that the motion is periodic, i.e. stable. The only conclusion, therefore, from this argument concerns the contribution of positive energy from the end conditions – which can be significant for a garden hose. This is clearly seen in Paidoussis & Issid (1974) who showed the appearance, for certain parametric combinations, of a coupled-mode flutter, *viz.* a pair of oscillatory modes even though the ends were pinned. They explained that there is frequency coalescence providing secular terms (linearly growing amplitude as a function of time) and hence the critical condition of flutter cannot be that of neutral stability (i.e. the motion is not periodic as assumed in the argument herein).

However, if we apply the loading over a part of the pipe, we see that there is clearly a possibility of instability due to the energy exchange at the end of the applied forcing, depending on the phasing of the fourth term in the right-hand side of (2.2). Indeed, the work done by this 'discontinuous' forcing will be non-zero. This is a similar flow-induced instability mechanism as in a cantilever pipe (Paidoussis 1998),

to render the system non-conservative, so that it can lose stability by flutter. When the fluid velocity U is sufficiently small, due to the effect of the Coriolis force the fluid provides negative energy, leading to damping of the pipe motion versus time. On the other hand, a flutter instability arises when $W_T > 0$, implying that the pipe is gaining energy from the fluid and hence its motion is amplified. So in this computationally convenient model, we enforce the fluid force to end at $L_m = 0.75L$, equivalent to discharging the fluid there, as if there the pipe discharges at that point the fluid in the local tangential direction. The vectoring of the fluid, i.e. as it changes direction since the pipe vibrates, is the mechanism of potential instability, as is also for a cantilever pipe. Since the effect of tension is also included, a non-dimensional fluid-tension parameter, I_p, is used to estimate the degree of the instabilities (Triantafyllou 1992):

$$I_p = \frac{m_a U^2}{T(1+e)/(e-0.125)}, \tag{2.3}$$

where $e = m_c/m_a$. Large values of I_p imply that the fluid has imparted more kinetic energy to the structure than can be supported by the tension; i.e. $I_p > 1$ for pipe conveying inviscid uniform flow (Triantafyllou 1992); otherwise, the tension effect dominates.

2.2. *Eigenvalue analysis of three models*

We also performed eigenvalue analysis of the system employing the simplified flow model, which is based on the added mass effect, expressed as:

$$m_c \frac{\partial^2 q}{\partial t^2} = \frac{\partial}{\partial s}\left(T\frac{\partial q}{\partial s}\right) - \frac{\partial^2}{\partial s^2}\left(EI\frac{\partial^2 q}{\partial s^2}\right) - m_a\left(\frac{\partial^2 q}{\partial t^2} + 2U\frac{\partial^2 q}{\partial t \partial s} + U^2\frac{\partial^2 q}{\partial s^2}\right). \tag{2.4}$$

Through the use of $\eta = q/L$, $\varepsilon = s/L$, $\tau = (EI/(m_c + m_a))^{1/2} t/L^2$, equation (2.4) can be rendered in dimensionless form:

$$\frac{\partial^2 \eta}{\partial \tau^2} + (u^2 - \alpha)\frac{\partial^2 \eta}{\partial \varepsilon^2} + 2u\sqrt{\beta}\frac{\partial^2 \eta}{\partial \tau \partial \varepsilon} + \frac{\partial^4 \eta}{\partial \varepsilon^4} = 0, \tag{2.5}$$

which employs the dimensionless system parameters:

$$u = \left(\frac{m_a}{EI}\right)^{1/2} LU, \quad \beta = \frac{m_a}{m_a + m_c}, \quad \alpha = \frac{TL^2}{EI}. \tag{2.6a–c}$$

Moreover, the dimensionless frequency ω is related to the dimensional circular frequency, Ω, by

$$\omega = \left(\frac{m_a + m_c}{EI}\right)^{1/2} \Omega L^2. \tag{2.7}$$

Equation (2.5) is discretized via the Galerkin method by using the eigenfunctions of a cantilevered beam for a cantilever pipe model, and sinusoidal functions for a pinned–pinned model, as basis and test functions (Paidoussis 1998).

Three systems, a cantilevered pipe, a pinned–pinned pipe with forcing over the entire length and a pipe with only partial ('discontinuous') fluid forcing are compared, see figure 2. In the cantilever model, it is seen that for dimensionless velocity

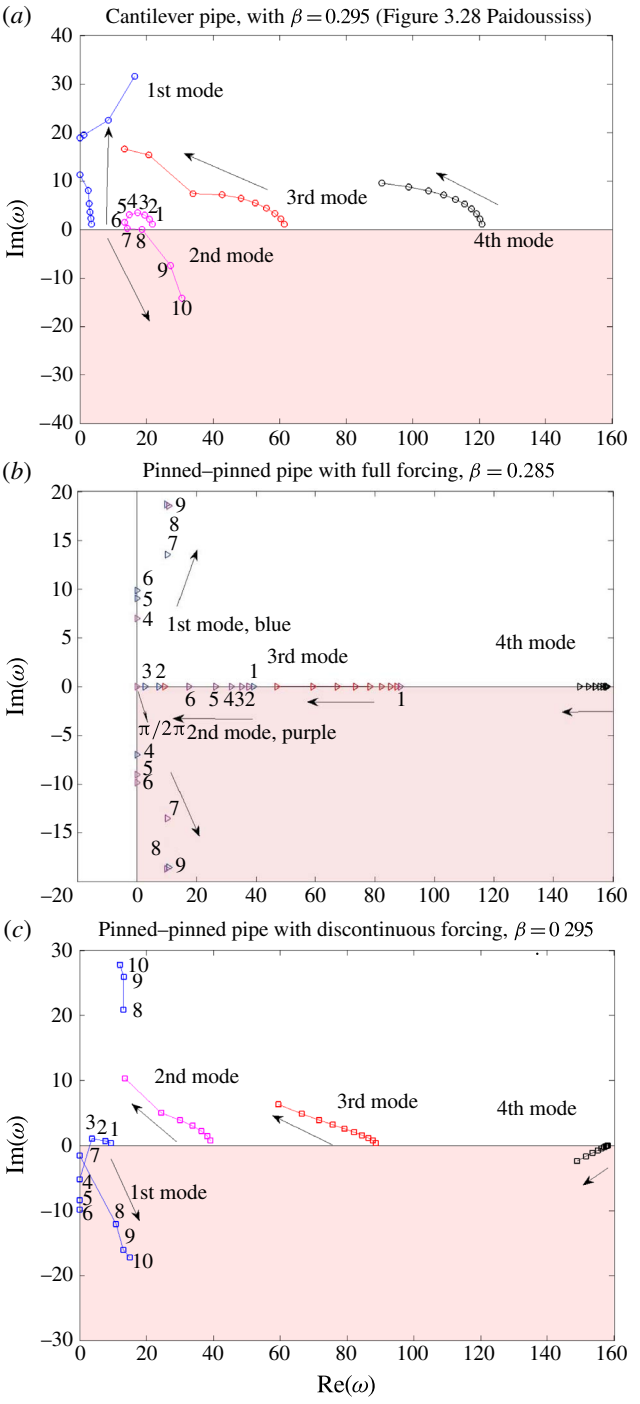

FIGURE 2. (Colour online) The complex frequency (ω) bifurcation diagrams of (a) a cantilever pipe with $L = 30D$, (b) a pinned–pinned pipe under 'full' forcing with $L = 40D$, (c) a pinned–pinned pipe under 'discontinuous' forcing with $L = 40D$. All are based on $\beta = 0.295$, $\alpha = 0$. The direction of arrow denotes increasing $u = 1 - 10$. The shaded area denotes the unstable modes.

$u \leqslant 7$, fluid damping applies to all modes of the system, i.e. $\mathrm{Im}(\omega) > 0$. Then, the system loses its stability to flutter in the second eigenfrequency after $u > 7$. For the pinned–pinned model under 'full' forcing, the eigenfrequencies are purely real and they decrease with increasing u, for $0 < u < \pi$; at $u = \pi$, the system loses stability in its first eigenfrequency by divergence (Paidoussis 1998). Although we have shown that for a periodic response the work W_t is zero from (2.2), this simply means that no energy is input from the pinned ends; we must recognize, however, that the system can develop secular growth (linear growth in amplitude versus time, for example), when the assumption of periodicity does not hold – otherwise one might conclude that there is a paradox that theory predicts that flutter cannot occur (Paidoussis & Issid 1974).

However, the instability of the pinned–pinned beam with continuous forcing is different from the instability of the same beam with discontinuous forcing; the latter resembles the instability of the garden hose, as energy may be gained from the end of the discontinuous forcing as well. Indeed, apart from divergence (buckling), the pinned–pinned pipe with 'full' forcing can only be subjected to a coupled-mode (first and second) flutter instability (Paidoussis & Issid 1974). On the other hand, for the 'discontinuous' forcing model, we found that both the first and fourth eigenfrequencies are dominant since their imaginary parts are negative. The fourth eigenfrequency will be excited at all velocity values while the first eigenfrequency is excited at $u \geqslant 4$ with either divergence or flutter response. The interaction of first and fourth eigenfrequency responses enriches the dynamics of the pinned–pinned pipe with the 'discontinuous' forcing model.

The 'discontinuous forcing model' and the cantilever model follow qualitatively the same instability path. However, due to the different boundary conditions used for these two models, equation (2.5) will present various bifurcation diagrams. For the 'discontinuous' forcing model, we have two pinned–pinned ends, while for the cantilever model, we have one fixed end and the other end free. We can see from figure 2(*a*,*c*) that the 'discontinuous forcing model' and cantilever model produce various responses. For the cantilever model, only the second eigenfrequency can be excited at $u \geqslant 8$, while the other three modes are suppressed since their imaginary parts are positive. The 'discontinuous' forcing model becomes unstable more easily by flutter because its critical dimensionless velocity is $u = 4$, lower than $u = 9$, that of the cantilever model. By further comparison, the mode excitation is shifted from the second mode in the cantilever model to combined first and fourth modes in the 'discontinuous' forcing model.

In summary, we have decided to use the 'discontinuous' forcing model due to its similarity with the cantilever model from work analysis and its faster computability.

2.3. *Fluid solver set-up*

For the flow DNS, the computational domain has the same size as the full length pipe. A 2-D grid of 260 quad elements with polynomial order $p = 5$ and 7 is used in the cross-flow (x, y) planes while 64 Fourier planes are employed in the axial z direction. As described in Newman & Karniadakis (1997), a no-slip condition is applied on the pipe surface. Fourier expansion implies spanwise periodicity of the flow and structural properties. Therefore, a constant force term F_z is applied along the axial direction to sustain the flow motion.

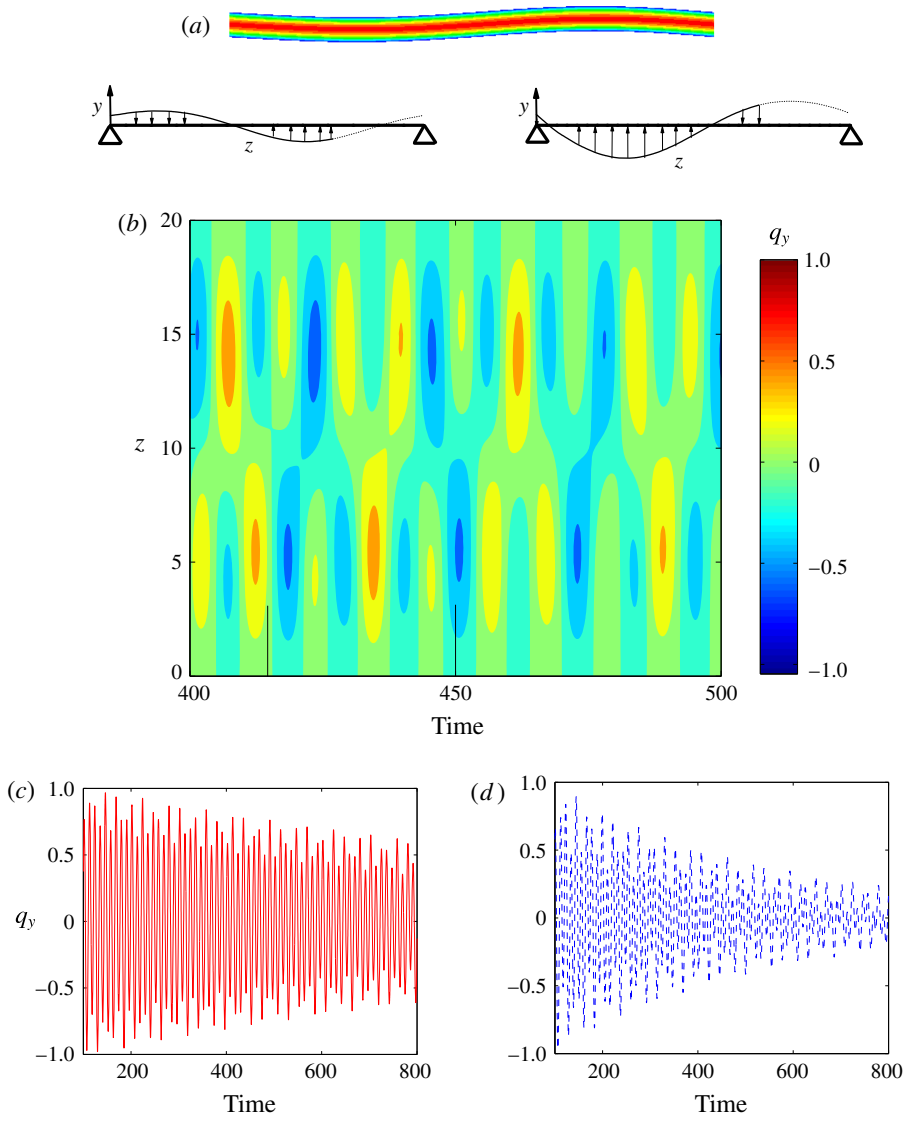

FIGURE 3. (Colour online) 'Discontinuous' forcing. (*a*) Simulation set-up, including the flow inside the pipe and for two instantaneous force distributions. (*b*) Selected time series of transverse displacement of pipe q_y, along the span, at $(Re, u, I_p) = (36, 1.16, 0.007)$. (*c*) Time traces of q_y at position L_m under 'full' forcing (red solid lines). (*d*) Time traces of q_y at position L_m under 'discontinuous' forcing (blue dashed lines).

3. Results and discussion

3.1. *Comparison of 'full' forcing model and 'discontinuous' forcing model*

First, we forced the pipe to vibrate in standing wave configuration for approximately 10 time periods and then let the pipe free to move with the 'discontinuous' forcing model, see (figure 3). The pipe has length $L/D = 20$. We first consider low values of the three important parameters $(Re, u, I_p) = (36, 1.16, 0.007)$. As we see in figure 3(*b*,*d*), the pipe returns gradually to a straight position (equilibrium),

as expected, but during the transient it maintains a standing wave motion in the transverse direction. Here we refer to this type of response as 'stationary status', to indicate that no matter what kind of initial response is imposed, the pipe will eventually return to a straight position. Moreover, in figure 3(*c*,*d*), we compare two cases with 'full' and 'discontinuous' forcing and follow the local oscillation at L_m; we see that in the latter case the amplitude decays faster since the fluid provides negative energy to the pipe system at low flow velocity, in agreement with the work analysis in the previous § 2.

3.2. *Phase diagram of flow–pipe instability*

Next, we focus on the dynamics of the self-excited pipe under 'discontinuous' forcing, as described above, with length $L/D = 40$. We performed simulations at two different (Re, u, I_p) parametric combinations, as shown in figure 4. They correspond to cases 1 and 2 in table 1. Figure 4(*a*,*c*) presents the displacement of the pipe in the transverse (y) direction along the axis in one period and figure 4(*b*,*d*) shows the trajectory of pipe in the (x, y) cross-flow plane at the position $z = 30D$, corresponding to the red vertical lines in (*a*,*c*). In the low (Re, u) and high I_p case, as shown in figure 4(*a*), an in-plane oscillation develops with the transverse response q_y excited in the first eigenfrequency of the pipe, but dominated by the second wavenumber, and with the pipe amplitude at the position L_m about $A_y = 1.7D$. However, in the high (Re, u) and low I_p case, an out-of-plane response develops, see figure 4(*c*), with transverse amplitudes of motion at the force discontinuity position L_m equal to $A_x = 3D$ and $A_y = 2D$. The vibratory response contains the first and fourth eigenfrequencies, as found through FFT (fast Fourier transform) analysis.

Furthermore, by recording the motion at the force discontinuity point (at L_m) in the $x - y$ plane, we see that we obtain in case 2 a distorted pentacle, instead of a straight line corresponding to an in-plane motion as in case 1, see figure 4(*b*,*d*). This difference in the dynamic response of the pipe is due to the flow bifurcation and has not been reported before. To explore the flow transition, we plot instantaneous flow patterns inside the pipe in figure 4(*e*,*f*) in terms of the transverse component of vorticity ω_x (left) and the axial velocity U (right) at different z stations $z = 0$, 10, 20, $30D$, from bottom to top. At the low $Re = 740$, the flow is stable and symmetric in the x-direction, consistent with $q_x = 0$. However, at high $Re = 1330$, the flow symmetry is broken, leading to a very well mixed flow at the cross-flow planes, as shown by the vorticity contours. We show in figure 4(*f*) the 2-D pipe motion resulting from the flow symmetry breaking, with the transverse motion now in the x-direction much higher than the y-direction, unlike the low Re case. From these results we see that the Reynolds number greatly influences the transition in the dynamic response of the pipe, from in-plane to combined in-plane and out-of-plane motion. Both responses can be observed in the garden-hose experiment, but the latter is more prevalent, as we usually operate at high Reynolds number.

Based on further DNS analysis, as reported above, we have constructed a phase diagram of flow–pipe instabilities in terms of three non-dimensional parameters (Re, u, I_p), see figure 5. Here, different colours denote different types of pipe motion: yellow points indicate stationary status, black points in-plane motion and red points out-of-plane motion. At higher values of (Re, u, I_p), the pipe is more prone to exhibit an out-of-plane motion. The hollow squares represent the response around $u = 14$ while the hollow triangles represent responses around $u = 10$ in this plot. We can see that at larger dimensionless fluid velocity $u = 14$, the threshold of $Re = 625$ is lower, compared with $Re = 1030$ at $u = 10$, for the transition of pipe motion from

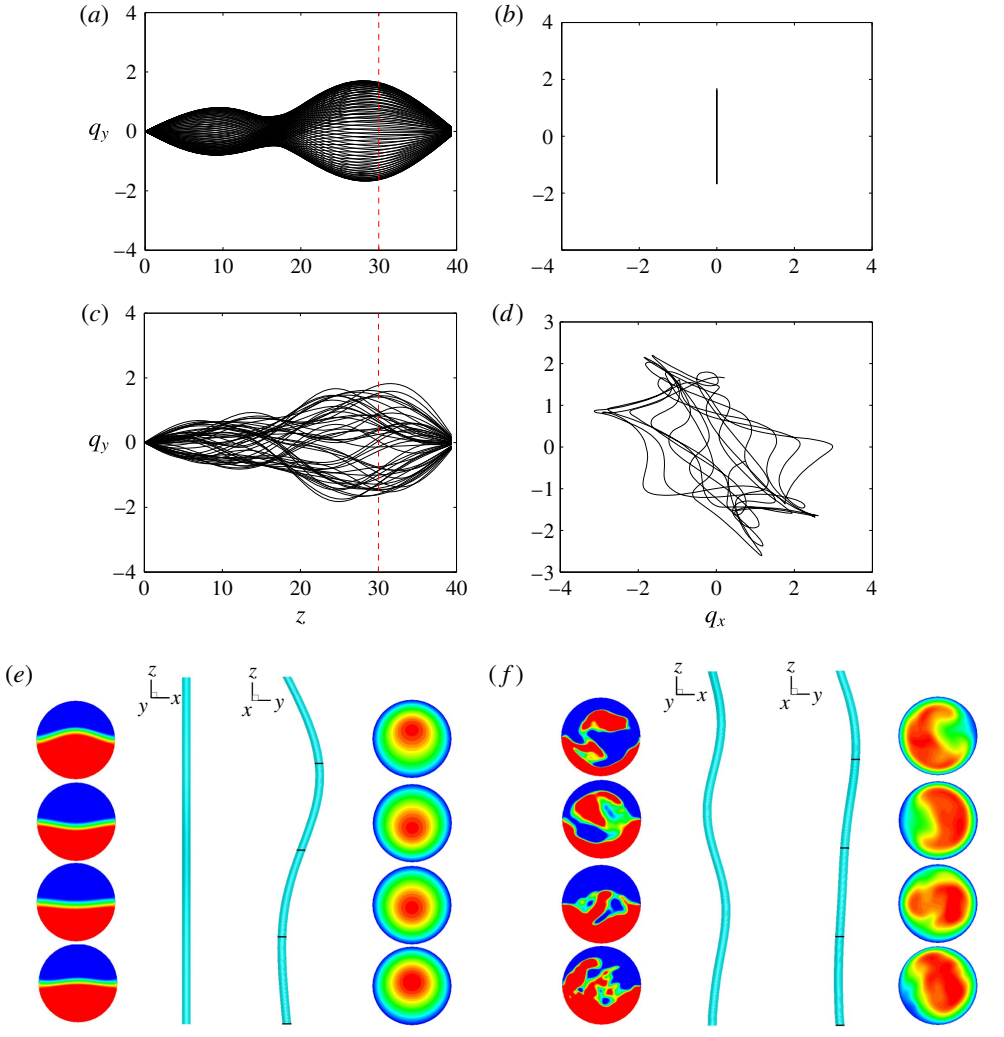

FIGURE 4. (Colour online) Flow–pipe instabilities at different (Re, u, I_p) groups obtained via DNS. (*a*,*b*,*e*) In-plane instability with $(Re, u, I_p) = (740, 7.9, 1.4)$, (*c*,*d*,*f*) out-of-plane instability with $(Re, u, I_p) = (1330, 14.2, 0.998)$. (*a*,*c*) Displacement of the pipe in the transverse (y) direction along the axis in one period. (*b*,*d*) Trajectory of the pipe in the (x, y) plane at the position $z = 30$, corresponding to the red vertical lines in (*a*,*c*). (*e*,*f*) Instantaneous shapes of the pipe and corresponding flow patterns (vorticity: $-2 \leqslant \omega_x \leqslant 2$ and axial velocity: $0 \leqslant U \leqslant 4$) at z stations $z = 0, 10, 20, 30D$ from bottom to top.

in-plane to out-of-plane motion. In the 3-D phase diagram, the solid circular points are all located within the grey-coloured plane cut, since they have the same value of fluid viscosity. If we plot the result on this plane cut, it will appear like the plot in figure 6, where we reduced the number of non-dimensional parameters to two, i.e. in terms of (Re, I_p), since the dimensionless velocity u is a linear function of Re. The values of the (Re, I_p) pair are varied through changing the fluid velocity and the pipe tension.

From figure 6, we can clearly see three different regimes, characterized by the Reynolds number and the relative tension of the pipe. The two dashed lines denote

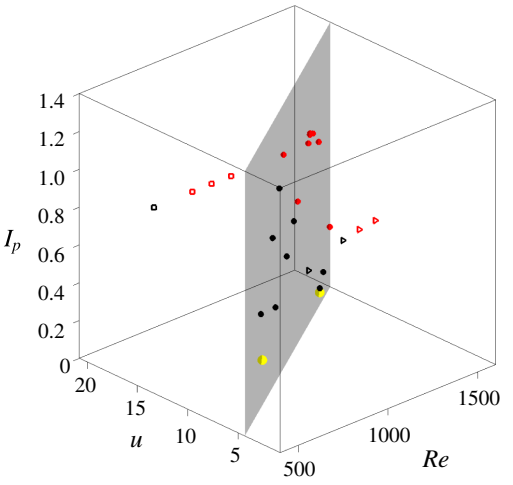

FIGURE 5. (Colour online) 3-D phase diagram of flow–pipe instability in terms of the group (Re, u, I_p). Different colours denotes different types of pipe motion. Yellow points: stationary status; black points: in-plane motion; red points: out-of-plane motion. All the solid circle points are located within the grey-coloured plane cut.

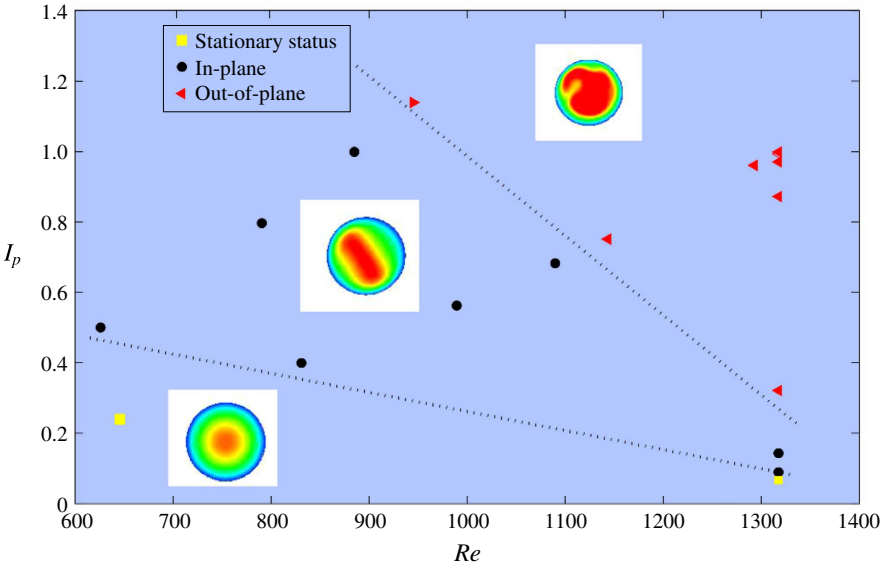

FIGURE 6. (Colour online) Phase diagram of flow–pipe instability in terms of the critical pair (Re, I_p). The two dashed lines denote two bifurcations, on the left from static to in-plane motion, and on the right from in-plane to out-of-plane motion.

regions of bifurcations, on the left from static to in-plane motion, and on the right from in-plane to out-of-plane motion. When the pipe remains stationary, the flow is stable and concentrates at the centre of pipe along the z axis. Under in-plane motion, the flow is no longer concentrated in the centre of the pipe along the z axis, but it is still symmetric along a specific direction, i.e. at 45° off the x-axis for the case with

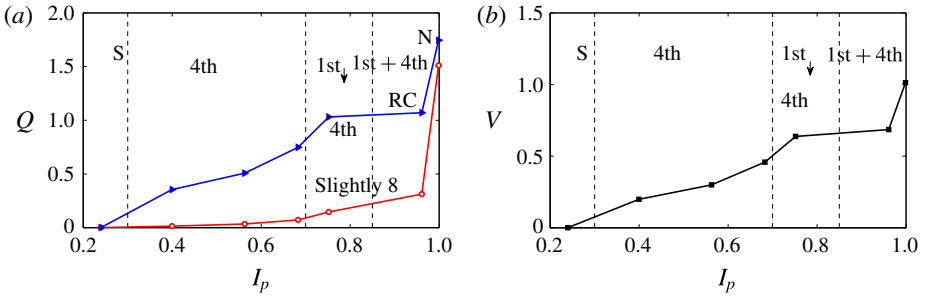

FIGURE 7. (Colour online) Bifurcation diagrams in terms of I_p. The corresponding Reynolds number varies as $646 \leqslant Re \leqslant 1330$. (*a*) L_2 norm of the transverse motion of pipe at different z stations; the red line with circles denotes the amplitude at the 'discontinuous' forcing position ($z = 0.75L$), while the blue line with triangles denotes the amplitude at the maximum position ($z \approx 0.825L$). (*b*) L_2 norm of total cross-flow velocity.

$(Re, I_p) = (990, 0.56)$. However, the flow symmetry is broken when the pipe follows an out-of-plane motion. An asymmetric form, lacking organization, characterizes the flow patterns when flow instability occurs, which leads to out-of-plane motion as well.

In general, the impact of Reynolds number Re on the transition of the motion is larger than the fluid-tension ratio I_p, i.e. at higher Reynolds number we can still achieve an out-of-plane motion even at a relatively lower I_p ratio. The variation of pipe motion is more sensitive at high Reynolds number. The range of I_p values for the presence of in-plane motion is narrower at higher Reynolds number, i.e. from $0.09 \leqslant I_p \leqslant 0.3$ at $Re = 1320$.

3.3. *Comparison of DNS and eigenvalue analysis*

In this subsection we present two bifurcation diagrams for the structure in terms of its transverse motion in the cross-flow (x, y) plane and for the flow, in terms of the total cross-flow velocity. Typically, a critical value of the dimensionless flow velocity, u, is adopted to determine the onset of flutter instability. Here, we analyse the same data sets as above with (Re, I_p) varying from $(646, 0.24)$ to $(1330, 0.998)$, as shown in figure 6. For these cases we maintain the same tension and flexible rigidity, and we vary the fluid velocity – see parameters for group 3 in table 1.

Figure 7 shows (*a*): the L_2 norm of the transverse motion of the pipe $Q = \sqrt{{q_x}^2 + {q_y}^2}$ at the discontinuity (red line with circles) and the maximum positions (blue line with triangles), and (*b*): the L_2 norm of the total cross-flow velocity $V = \sqrt{u^2 + v^2}$. Based on the existing data in figure 7, $I_p = 0.4$ and $I_p = 0.75$ are the two critical values for the onset of in-plane and out-of-plane motion, respectively. In particular, $I_p = 0.4$ is the critical value for the onset of flow instability since the total cross-flow velocity becomes non-zero, denoting that the transverse component of the flow velocity is affecting greatly the pipe motion. The post-critical dynamics of the system (i.e. the dynamics beyond the threshold of the first instability) is very rich. The trajectories of displacement at $L_m = 0.75L$ (in red) and $z = 0.825L$ (in blue) at (x, y) plane for different (Re, I_p) pairs are presented in figure 8. At the discontinuous position, with increasing (Re, I_p) values, the pipe exhibits finite displacement response, see figure 8(*a–f*). It varies from a straight line to a figure-'8' shape, then a circular motion and eventually a pentacle motion. The transition from linear motion to the

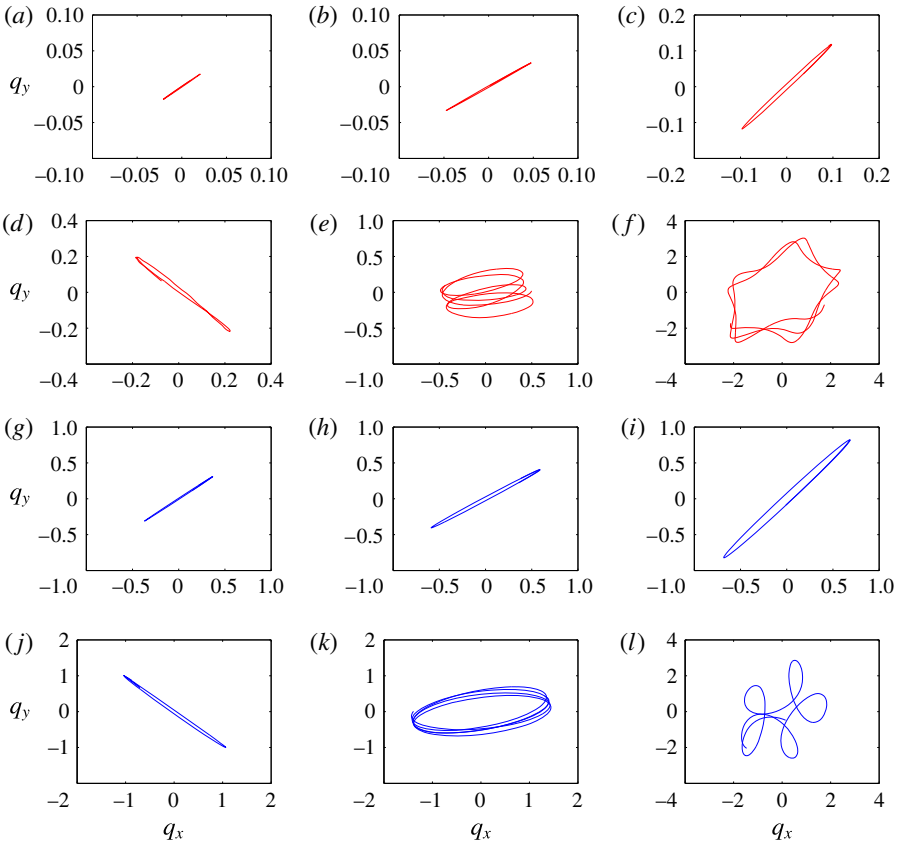

FIGURE 8. (Colour online) Trajectories of the displacement of the pipe at $L_m = 0.75L$ (red) and $z = 0.825L$ (blue) in (x, y) plane for different (Re, I_p) pairs. (a,g) $(Re, I_p) = (833, 0.4)$, (b,h) $(Re, I_p) = (990, 0.56)$; (c,i) $(Re, I_p) = (1080, 0.68)$; (d,j) $(Re, I_p) = (1140, 0.75)$; (e,k) $(Re, I_p) = (1290, 0.97)$; (f,l) $(Re, I_p) = (1330, 0.998)$.

figure-'8' shape corresponds to the flow transition from a symmetric state to a disorganized state, with the change of (Re, I_p) from (1080, 0.68) to (1140, 0.75). From figure 8(*g–l*), we can see that for the first three cases, with in-plane instability, the pattern of the trajectory at the maximum vibration response position is similar to that at the discontinuous position, and with larger amplitude. But when $I_p \geqslant 0.75$, with out-of-plane instability, due to the nonlinear effect, the vibration response and the corresponding trajectory in the (x, y) plane vary along the pipe axis. Especially, in the case of $(Re, I_p) = (1330, 0.998)$, we can see a nutation motion at the maximum response position, see figure 8(*l*).

Moreover, a spatio-temporal spectral analysis of the transverse displacement is presented in figure 9. The yellow vertical dashed lines denote the natural frequencies, identified by $f_n = ((n^2\pi\sqrt{EI/(m+m_a)})/2L^2)\sqrt{(1+(TL^2/EI\pi^2n^2))}$, where $f_1 = 0.018$, $f_2 = 0.039$, $f_3 = 0.0642$, $f_4 = 0.961$. The wavenumbers of selected sine Fourier modes are indicated by purple horizontal dashed lines. It is seen that only the fourth eigenfrequency is excited if $I_p \leqslant 0.68$. At $I_p = 0.75$, the first eigenfrequency is excited in the beginning but eventually the vibration is shifted to the fourth eigenfrequency. Subsequently, for even higher values, i.e. $I_p \geqslant 0.97$, both the first

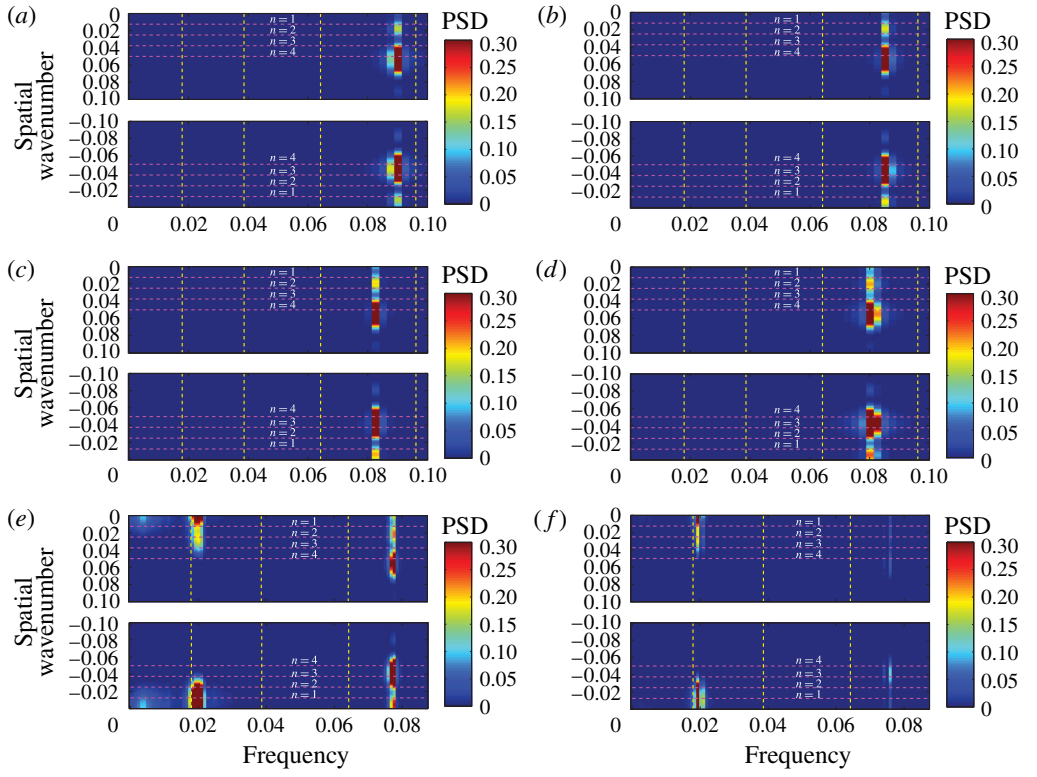

FIGURE 9. (Colour online) Spatio-temporal spectral analysis of vertical displacement q_y at different (Re, I_p) pairs, taken from group 3 cases. The yellow vertical dashed lines denote the natural frequencies identified by $f_n = ((n^2\pi\sqrt{EI/(m+m_a)})/2L^2)\sqrt{(1+(TL^2/EI\pi^2n^2))}$, where $f_1 = 0.018, f_2 = 0.039, f_3 = 0.0642, f_4 = 0.0961$. The wavenumbers of selected sine Fourier modes are indicated by purple horizontal dashed lines. (*a*) $(Re, I_p) = (833, 0.4)$, (*b*) $(Re, I_p) = (990, 0.56)$, (*c*) $(Re, I_p) = (1080, 0.68)$, (*d*) $(Re, I_p) = (1140, 0.75)$, (*e*) $(Re, I_p) = (1290, 0.97)$, (*f*) $(Re, I_p) = (1330, 0.998)$.

and fourth eigenfrequencies are (nearby fourth eigenfrequency), we see that it is decreasing with I_p, from $f_e = 0.09$ at $I_p = 0.4$ to $f_e = 0.076$ at $I_p = 0.998$.

In parallel with the DNS parametric study, we performed an eigenvalue analysis of the pinned–pinned pipe with 'discontinuous' added mass forcing and using the same parameters – see figure 10. For all cases, the second and third eigenfrequency responses are reduced, and increasing I_p reduces them further. At lower I_p ratio, $I_p \leqslant 0.75$, the fourth eigenfrequency is dominant in the vibration response. However, at higher I_p ratio, $I_p \geqslant 0.97$, both the first and fourth eigenfrequencies are excited, while the first eigenfrequency response may even be associated with buckling of the pipe since its value becomes zero. However, in DNS (and in experiments), this buckling behaviour is not observed because of nonlinear effects.

In the following, we plot the instantaneous predominant frequency as a function of time and space in figure 11 to explain the nonlinear effect on the frequency response. It has been shown in figure 9 that several wavenumbers can contribute to the vibration response. The question is whether the response is instantaneously mono-frequency, with a shifting frequency in time or it is multi-frequency at all times. Obviously, the

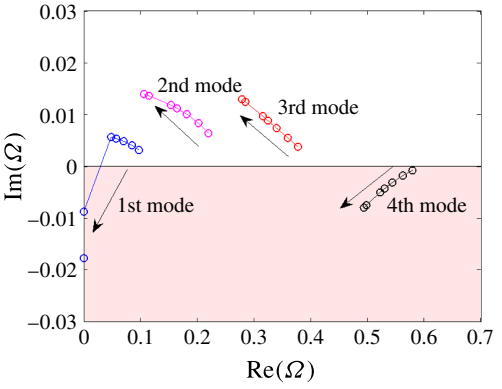

FIGURE 10. (Colour online) The complex frequency (Ω) diagrams (based on (2.4)) for a pinned–pinned pipe under 'discontinuous' forcing with parameters for group 3 cases. The direction of the arrow denotes increasing I_p by varying $U = 2.15$–4.4. The shaded area denotes unstable modes.

temporal variation of the dominant frequency does not occur simultaneously along the entire span in our study, see figure 11.

According to the previous linear theory analysis, the frequency response will be constant both in time and space with value ($f_4 = 0.08$) at lower I_p cases. On the other hand, at higher I_p ratio, the frequency responses should contain two values: $f_1 = 0.0$ and $f_4 = 0.08$ both in time and space since both first and fourth modes are excited. However, we can see that at smaller $I_p = 0.56$, a weak nonlinearity effect manifests itself in the frequency response, since the colour legend is filled by grey and has little white, corresponding to the frequency value range of (0.08, 0.11), see figure 11(*a–d*). This nonlinear effect becomes stronger at higher I_p with a wider range of frequency value response, as shown in figure 11(*e–f*). The lowest frequency value becomes $f_1 = 0.02$ instead of zero frequency where the bucking would exist in the linear analysis.

Furthermore, we analyse the synchronization of the transverse motions q_x and q_y using DNS, identifying the phase angle between q_x and q_y in figure 12. The phase difference Φ_{xy} is constant for $I_p \leqslant 0.68$, where the trajectory of the pipe motion is an in-plane motion, see figure 8(*a–c*, *g–i*). For the other cases with $I_p \geqslant 0.75$, the trajectory of the pipe follows out-of-plane patterns since the phase difference Φ_{xy} for these cases is time and space dependent. In summary, the excitation frequencies obtained by the eigenvalue analysis and the modal analysis from DNS results match closely.

4. Conclusion

The present study elucidates the flow mechanisms involved in the onset of instability of fluid-conveying pipes that are free to vibrate. We study the system using fully resolved simulation, in parallel with eigenvalue analysis of the system employing a simplified fluid problem, to place the results in context with the results from previous analyses. We constructed a 3-D phase diagram of the flow–pipe instability in terms of the group of three basic parameters (Re, u, I_p), whereas typically only u and I_p have been used before, to study the dynamic motion of the pipe. The Reynolds number

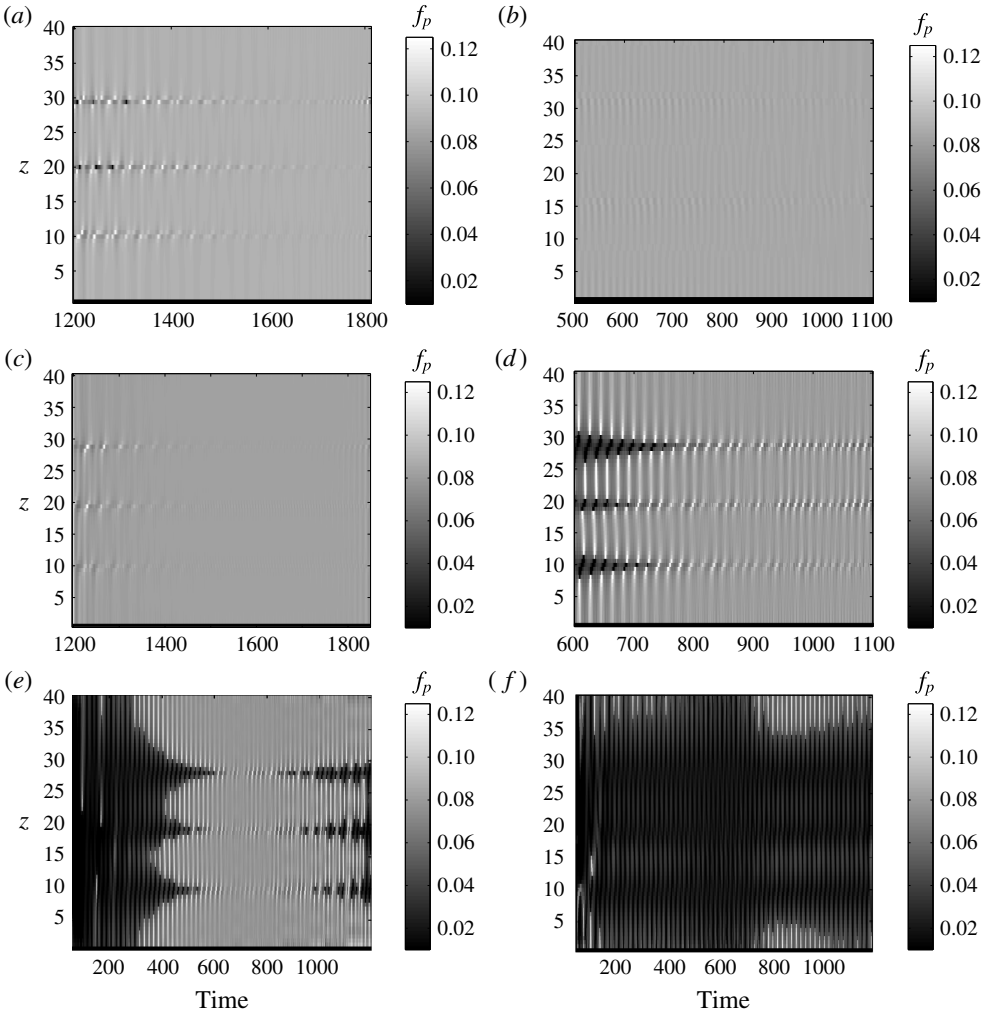

FIGURE 11. Dominant frequency of vertical displacement as a function of time along the cylinder span at different (Re, I_p) pairs, corresponding to figure 9. (*a*) $(Re, I_p) = (833, 0.4)$, (*b*) $(Re, I_p) = (990, 0.56)$, (*c*) $(Re, I_p) = (1080, 0.68)$, (*d*) $(Re, I_p) = (1140, 0.75)$, (*e*) $(Re, I_p) = (1290, 0.97)$, (*f*) $(Re, I_p) = (1330, 0.998)$.

Re plays a very important role in the transition of the pipe motion to also include out-of-plane motion, while the value of u and the I_p ratio determine the amplitude of the vibration. For example, in figure 4, we show that even for very large I_p values, the oscillation is not self-sustained if the Reynolds number is low. Moreover, the precise flow patterns inside the pipe determine the type of induced motion. Even for unsteady flow, symmetry along one direction leads to in-plane motion, whereas breaking of the flow symmetry results in out-of-plane motion. In summary, above a threshold Reynolds number, complex flow patterns result, because there is continuous generation of new vorticity due to the pipe wall acceleration, and subsequent shedding of vorticity in a confined space, *viz.* the pipe interior.

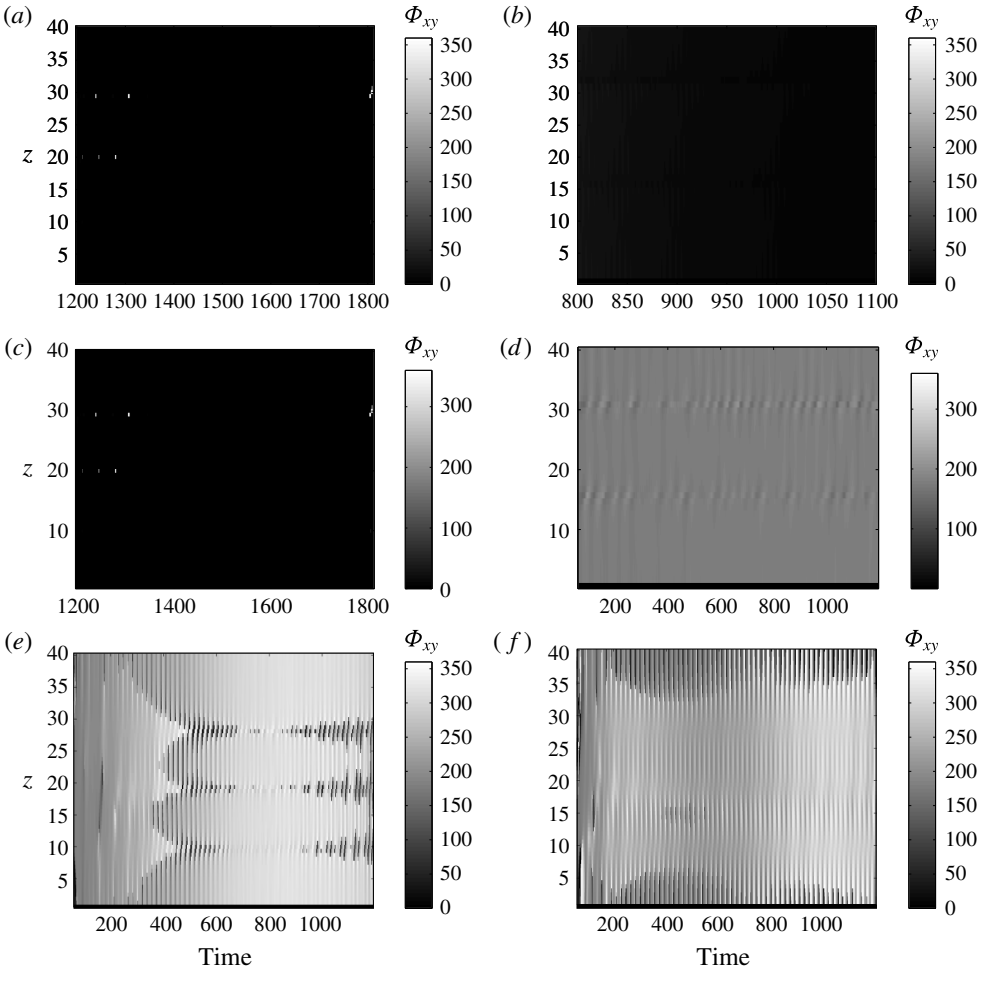

FIGURE 12. Temporal evolution of phase angle difference between horizontal and vertical displacements $\Phi_{xy} = \mathrm{mod}\,(p\Phi_x - q\Phi_y, 2\pi)\cdot 360$, with $(p, q) = (1, 1)$, along the cylinder span at different (Re, I_p) pairs, corresponding to figure 9. (*a*) $(Re, I_p) = (833, 0.4)$, (*b*) $(Re, I_p) = (990, 0.56)$, (*c*) $(Re, I_p) = (1080, 0.68)$, (*d*) $(Re, I_p) = (1140, 0.75)$, (*e*) $(Re, I_p) = (1290, 0.97)$, (*f*) $(Re, I_p) = (1330, 0.998)$.

Acknowledgements

The authors gratefully acknowledge support by the Chevron-MIT University Partnership Program. FFX also wants to thank Dr. R. Bourguet of the University of Toulouse for providing the FFT analysis tools.

REFERENCES

ASHLEY, H. & HAVILAND, G. 1950 Bending vibrations of a pipe line containing flowing fluid. *Trans. ASME J. Appl. Mech.* **17** (3), 229–232.

BENHAMOU, B., LANEVILLE, A. & GALANIS, N. 2004 Transition to turbulence: the case of a pipe in radial oscillations. *Intl. J. Therm. Sci.* **43** (12), 1141–1151.

BENJAMIN, T. B. 1961*a* Dynamics of a system of articulated pipes conveying fluid. I: theory. *Proc. R. Soc. Lond.* A **261** (1307), 457–486.

BENJAMIN, T. B. 1961*b* Dynamics of a system of articulated pipes conveying fluid. II: experiments. *Proc. R. Soc. Lond.* A **261** (1307), 487–499.

BOURGUET, R., KARNIADAKIS, G. E. & TRIANTAFYLLOU, M. S. 2011 Vortex-induced vibrations of a long flexible cylinder in shear flow. *J. Fluid Mech.* **677**, 342–382.

BOURGUET, R., KARNIADAKIS, G. E. & TRIANTAFYLLOU, M. S. 2013 Distributed lock-in drives broadband vortex-induced vibrations of a long flexible cylinder in shear flow. *J. Fluid Mech.* **717**, 361–375.

BOURRIÈRES, F. J. 1939 *Sur un phénomène d'oscillation auto-entretenue en mécanique des fluides réels*. E. Blondel La Rougery.

CROS, A., ROMERO, J. A. R. & FLORES, F. C. 2012 Sky dancer: a complex fluid-structure interaction. In *Experimental and Theoretical Advances in Fluid Dynamics*, pp. 15–24. Springer.

DOARÉ, O. & DE LANGRE, E. 2002 The flow-induced instability of long hanging pipes. *Eur. J. Mech. (*A*/Solids)* **21** (5), 857–867.

EVANGELINOS, C. & KARNIADAKIS, G. E 1999 Dynamics and flow structures in the turbulent wake of rigid and flexible cylinders subject to vortex-induced vibrations. *J. Fluid Mech.* **400**, 91–124.

GREGORY, R. W. & PAIDOUSSIS, M. P. 1966 Unstable oscillation of tubular cantilevers conveying fluid. I: theory. *Proc. R. Soc. Lond.* A **293** (1435), 512–527.

GUO, C. Q., ZHANG, C. H. & PAÏDOUSSIS, M. P. 2010 Modification of equation of motion of fluid-conveying pipe for laminar and turbulent flow profiles. *J. Fluids Struct.* **26** (5), 793–803.

IBRAHIM, R. A. 2010 Overview of mechanics of pipes conveying fluidsâ. Part I: fundamental studies. *Trans. ASME: J. Press. Vessel Technol.* **132** (3), 034001.

KARNIADAKIS, G. E. & SHERWIN, S. J. 2013 *Spectral/hp Element Methods for Computational Fluid Dynamics*, 2nd edn. Oxford University Press.

NEWMAN, D. J. & KARNIADAKIS, G. E. 1997 A direct numerical simulation study of flow past a freely vibrating cable. *J. Fluid Mech.* **344**, 95–136.

PAIDOUSSIS, M. P. 1998 *Fluid-Structure Interactions: Slender Structures and Axial Flow*. vol. 1. Academic.

PAIDOUSSIS, M. P. 2004 *Fluid-Structure Interactions: Slender Structures and Axial Flow*. vol. 2. Academic.

PAIDOUSSIS, M. P. & ISSID, N. T. 1974 Dynamic stability of pipes conveying fluid. *J. Sound Vib.* **33** (3), 267–294.

TRIANTAFYLLOU, G. S 1992 Physical condition for absolute instability in inviscid hydroelastic coupling. *Phys. Fluids* A **4** (3), 544–552.